Effect of the anchoring strength on the phase behaviour of discotic liquid crystals under face-on confinement

Effect of the anchoring strength on the phase behaviour of discotic liquid crystals under face-on confinement

Daniel Salgado-Blanco *[1], Enrique Díaz-Herrera[2] and Carlos I. Mendoza[3]

[1]Cátedras CONACyT - Centro Nacional de Supercómputo, Instituto Potosino de Investigación Científica y Tecnológica, Camino a la Presa San José 2055, 78216, San Luis Potosí, México
[2]Departamento de Física, Universidad Autónoma Metropolitana-Iztapalapa, Ave. San Rafael Atlixco 186, Col. Vicentina, 09340 México, Ciudad de México, Mexico
[3]Instituto de Investigaciones en Materiales, Universidad Nacional Autónoma de México, Apdo. Postal 70-360, 04510 México, Ciudad de México, Mexico

Abstract

In this study we have performed molecular dynamics simulations to study a Gay-Berne discotic fluid confined in a slab geometry for a fixed confinement length. Four different anchoring strengths with a homeotropic (face-on) configuration were studied. We found that changing the anchoring strength changes the normal component of the stress tensor, which in turn changes the density of the system's bulk. This phenomenon leads to a shift in the isotropic-nematic transition temperature. We observe that the temperature regions where the nematic phase is present diminishes as the anchoring strength increases. The anchoring strength also affects the nematic-columnar coexistence temperature-region: it spans over more temperatures at higher anchoring strengths.

1 Introduction

Liquid crystals (LC) are composed of molecules with anisotropic shape and/or interactions, which display interesting phenomena due to their ability to display mesophases, or intermediate phases between the completely disordered isotropic liquid, where all positions and orientations are equivalent, and the most ordered crystalline phase, where the positions and orientations of the molecules are fixed. This characteristic is relevant if not the dominant factor for many of their

*E-mail: daniel.salgado@ipicyt.edu.mx

electronic, optical and magnetic properties [1–4], or their particular behaviour in flow [5–7].

As it turns out, these anisotropic systems are strongly sensitive to interfacial interactions. Indeed, upon confinement, a delicate energetic balance between adhesive (LC-surface interaction) and cohesive (intermolecular interactions) forces occurs, subject to thermodynamic conditions. Understanding the different phenomena occuring for liquid crystals in confinement presents a fundamental problem [8–10], and are critical to many LC technologies which involve a direct interaction with surfaces [11–13].

Different numerical studies have been made to understand this process where the LC's are forced to arrange themselves, or self-assemble, at conditions of confinement. Most of these studies have been dedicated to the case of a fluid composed of rod-like molecules (prolates) [10,14–19], and few of them have focused on the effect of confining a discotic liquid crystal (oblates) [20–24]. A discotic liquid crystal (DLC) consists of disc-shaped mesogens, composed, as a majority, of polycyclic aromatic cores surrounded by plural number of flexible aliphatic chains [25]. While prolates tend to form smectic phases, where the particles align themselves in layers that posses a preferential orientation, oblates tend to arrange themselves into columnar phases, due to strong π-π interactions [4]. This unidirectional arrangement, coupled with its promising charge carrier mobilities and the fact that they can be considered as organic semiconductors, make the DLC a particularly interesting candidate for applications on the photovoltaic industry [4,26,27]. Nevertheless, more attention is needed to complete design principles for DLC's in a confined environment that improve the handling of its orientational order.

A common strategy to achieve a desired orientation, or improve the orientational order on confined LC systems, is by the manipulation of the local order of particles adsorbed into the solid surfaces, or anchoring of the walls; this local order promoted by the walls is known to induce such order on the rest of the fluid via elastic forces [28]. The orientation of molecules within the surface can be manipulated by various means, such as photoallignment techniques [29], surface chemistry [30] and topographic patterning [31], only to name a few. Three broad classes of anchorings can be used to describe the type of alignment: planar, homeotropic and tilted. In the first case, the director is parallel to the surface, while a homeotropic anchoring means that the director lies normal to the surface, and, in the last case, the director is tilted with respect to the surface. In the specific case of a homeotropic anchoring, in which the discs lie "face-on" on the surface, a particular benefit for the performance in photovoltaic cells is expected [25].

Hence, the global and local structure of a confined DLC could be enormously affected by the nature of the DLC-wall interaction. For instance, it could be expected that imposing a strong anchoring represents an improvement in the global molecular alignment of a confined DLC, this is, that by increasing the adhesive force of the confining surface, not only the particles adjacent to the wall improved their alignment, but that they also induce such improved order, via elastic forces, at the bulk region of the DLC where the direct interaction

of the walls is no longer present. Herein we address such question, about the importance of the anchoring strength with regard to the bulk behaviour, by performing molecular dynamics simulations of four systems confined by two parallel walls (slab geometry), separated by a fixed distance and with different anchoring strengths, while exploring different temperatures.

The rest of the paper is structured as follows: Section 2 presents the model used to mathematically describe our system and the details of the molecular simulation employed, Section 3 contains the results for all the confined systems studied in this work and the corresponding results for the unbounded system. Finally, the concluding remarks are included in Section 4.

2 Model description and simulations

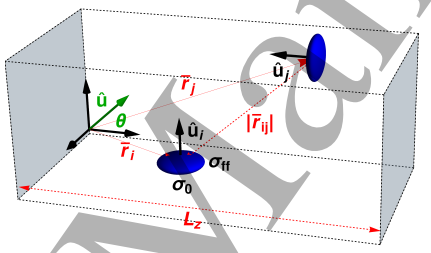

Figure 1: Schematic view of the system under study. Notice at the origin a green unitary vector $\hat{u}$ which forms an angle θ with the vector normal to the wall (z direction). This angle will turn useful in the definition of a disc-wall potential which is angle-dependant.

2.1 Disc-disc and disc-wall interaction

The system consists of a discotic liquid crystal confined in a rectangular slab, whose walls are separated by a fixed distance $L_z^* = L_z/\sigma_0$ with σ_0 the diameter of the discogen, as seen in Fig. 1. The particle-particle interaction is defined by a Gay-Berne pair potential [32]

$$U(\hat{\mathbf{u}}_i, \hat{\mathbf{u}}_j, \hat{\mathbf{r}}_{ij}) = 4\epsilon(\hat{\mathbf{u}}_i, \hat{\mathbf{u}}_j, \hat{\mathbf{r}}_{ij})(\Xi_{ij}^{-12} + \Xi_{ij}^{-6}), \tag{1}$$

where $\hat{\mathbf{r}}_{ij} = \mathbf{r}_{ij}/r_{ij}$ is the unit vector that connects the centers of particles i and j, $\hat{\mathbf{u}}_x$ is the unit vector along the principal axes of discogen x, and ϵ is the strength anisotropy function (see below). In the last expression, Ξ is an orientation dependant function defined by

$$\Xi_{ij} = \frac{\sigma_{ff}}{r_{ij} - \sigma(\mathbf{u}_i, \hat{\mathbf{u}}_j, \hat{\mathbf{r}}_{ij}) + \sigma_{ff}}, \tag{2}$$

where σ_{ff} represents the thickness of the discogen. The contact distance between particles i and j, is given by

$$\sigma(\hat{\mathbf{u}}_i, \hat{\mathbf{u}}_j, \hat{\mathbf{r}}_{ij}) = \sigma_0 \Gamma^{-\frac{1}{2}}(\chi) \tag{3}$$

where the molecular anisotropy parameter χ, is defined as

$$\chi = \frac{\kappa^2 - 1}{\kappa^2 + 1} \tag{4}$$

with $\kappa = \sigma_{ff}/\sigma_0$. The function $\Gamma(\omega)$ is defined by

$$\Gamma(\omega) = 1 - \omega \left[\frac{c_i^2 + c_j^2 - 2\omega c_i c_j c_{ij}}{1 - \omega^2 c_{ij}^2} \right], \tag{5}$$

with $c_i \equiv \mathbf{u}_i \cdot \hat{\mathbf{r}}_{ij}$, $c_j \equiv \mathbf{u}_j \cdot \hat{\mathbf{r}}_{ij}$, and $c_{ij} \equiv \mathbf{u}_i \cdot \mathbf{u}_j$. Finally, we define the strength anisotropy function as:

$$\epsilon(\hat{\mathbf{u}}_i, \hat{\mathbf{u}}_j, \hat{\mathbf{r}}_{ij}) = \epsilon_0 \epsilon_1^{\nu}(\hat{\mathbf{u}}_i, \hat{\mathbf{u}}_j) \epsilon_2^{\mu}(\hat{\mathbf{u}}_i, \hat{\mathbf{u}}_j, \hat{\mathbf{r}}_{ij}), \tag{6}$$

with μ and ν adjustable exponents,

$$\epsilon_1(\hat{\mathbf{u}}_i, \hat{\mathbf{u}}_j) = \left[1 - \chi^2 c_{ij}^2\right]^{-\frac{1}{2}}, \tag{7}$$

and

$$\epsilon_2(\hat{\mathbf{u}}_i, \hat{\mathbf{u}}_j, \hat{\mathbf{r}}_{ij}) = \Gamma(\chi'), \tag{8}$$

where

$$\chi' = \frac{(\kappa')^{\frac{1}{\mu}} - 1}{(\kappa')^{\frac{1}{\mu}} + 1}, \tag{9}$$

and $\kappa' = \epsilon_e/\epsilon_f$. Here ϵ_e represents the potential well depth for an edge-edge configuration, and ϵ_f the potential well depth for a face-face configuration. Making $\kappa' = 0.2$ in the potential favors the face-face configuration between the discs, so that the nematic and columnar phases are promoted (Figure 2a).

We will express a set of parameters for the Gay-Berne potential using the notation GB(κ, κ', μ, ν), as proposed by Bates and Luckhurst [33]. The parametrization of the system investigated in this study is GB(0.345, 0.2, 1.0, 2.0), an aspect ratio regularly chosen due to its similar proportions with a molecule with a triphenylene core [34]. Notice that this set of parameters promotes the formation of columns of discs, since the strongest attraction between nematogens happens when their axis are parallel to each other and to the vector that connects their centers.

The wall-disc interaction is also modeled with a Gay-Berne potential [24] of the form:

$$\begin{aligned} V(z, \theta) = & \epsilon_w \left[\frac{2}{15} \left(\frac{\sigma_{ff}}{z - z_{shift}(\theta)} \right)^9 - \left(\frac{\sigma_{ff}}{z - z_{shift}(\theta)} \right)^3 \right] \\ & \times \left[1 + A P_2(\cos(\theta))\right], \end{aligned} \tag{10}$$

where $P_2(x) = \frac{1}{2}(3x^2 - 1)$ is the second order Legendre polynomial, ϵ_w is an energy prefactor which determines the strength of the anchoring with respect to the disc-disc interaction, and θ is the angle between the vector normal to the wall and the vector along the principal axes of a given discogen (see Fig. 1). The function z_{shift} determines the wall-disc contact distance and is defined as

$$z_{shift}(\theta) = 0.5\left[\sigma_0\left(1 - \frac{2\chi}{1+\chi}\cos^2(\theta)\right)^{-\frac{1}{2}} - \sigma_{ff}\right] \quad (11)$$

The advantage of this model for the wall-disc interaction over other existing in the literature is that it allows calculating the forces and gorques in an easy way, hence facilitating a molecular dynamics simulations. It also allows changing the depth of the magnitude of the anchoring energy, as well as the preferred anchoring orientation. The type of anchoring at the walls is determined by the value of the parameter A. For example, $A = -0.5$ promotes a planar or edge-on anchoring, while $A = 1.0$ encourages an homeotropic or face-on anchoring. In this work, we set $A = 1.0$ for all cases and used four different values of ϵ_w (namely, $1, 5, 10$ and 15), this is, we set a face-on anchoring and choose four differente anchoring strengths, as depicted in Fig. 2b where we plot $V(z^*, \theta = 0)$ as a function of $z^* = z/\sigma_0$, the distance of the particle to the wall, for $\epsilon_w = 1, 5, 10$ and 15 which are depicte by the black, red, blue and green lines, respectively. As we will show in the discussion section, this values for ϵ_w, together with the rest of the system parameters, represent configurations within typical experimental setups [17, 35, 36].

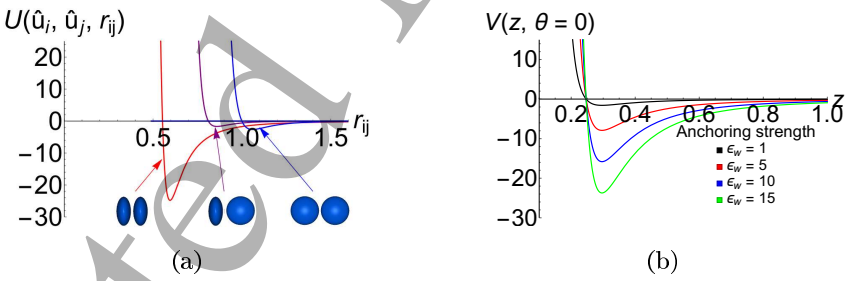

Figure 2: (a) Disc-disc interaction potential as given by Eq. 1 for the system GB(0.345,0.2,1.0,2.0). The red line corresponds to the face-face interaction, the blue line to the edge-edge interaction and the purple line to the edge-face interaction. A schematic view of a pair of discogens interacting are included in the same order in which the lines of the potential appear (from left to right: face-face, edge-face and edge-edge). (b) Wall-disc interaction potential as given by Eq. 10 with the parameters set in this study. The black, red, blue and green line corresponds to a value of $\epsilon_w = 1, 5, 10$ and 15, respectively. In the four cases, the graphics represents a particle in a face-on configuration ($\theta = 0$) approaching to a wall promoting a face-on anchoring ($A = 1.0$).

2.2 Simulation details

Molecular Dynamics simulations have been carried out on an ensemble of 20000 particles inside of a parallelepipedic box of variable volume V. The simulation box presents periodic boundary conditions along the x and y directions and is limited along the z axis by two walls which promote an homeotropic or face-on anchoring. In this simulations the Nosé-Hoover thermostat/barostat [37] couple was used to held fixed the temperature of the system and its average tangential components of the stress tensor P^*_{xx} and P^*_{yy}, with $P^*_{xx} = P^*_{yy} = 25$, and where each component of the stress tensor was determined by the standard virial route. This value of the tangential pressure is taking in analogy to the value of the normal pressure applied on a similar study developed by Bellier-Castella *et al.* [24]. Nevertheless, our intention was to study the effect of varying the anchoring strength in a slab geometry, where the distance between the walls remained fixed, and, hence, in the ensemble we used, only the x-y area of the box was allowed to fluctuate, such as in the ensembles used in refs [38–40]. In this regard it is important to notice that, given that in this ensemble the normal component of the stress tensor is set free, the system's pressure does not remain constant. This will turn of primary importance when we compare the results for systems with different anchoring strengths.

The Nosé-Hoover thermostat constant was set at $Q_t = 10$, while the barostat constant used was $Q_p = 1000$. These values of the thermostat and barostat masses are similar to those used in Ref. [37], although a small adjustment was applied to the thermostat mass in order to avoid strong fluctuations of the kinetic energy. We have used σ_0 and ϵ_0 as length and energy units, respectively, and standard reduced units ($T^* = k_B T/\epsilon_0$, $P^* = P\sigma_0^3/\epsilon_0$ and $\rho^* = \rho\sigma_0^3$, where k_B stands for the Boltzmann constant) for the rest of the system parameters. Equations of translational and orientational dynamics were integrated using the velocity-Verlet algorithm with a reduced time step of $\delta t = \delta t(\sigma_0^2 m/\epsilon_0)^{-\frac{1}{2}} = 0.0015$ (where $m = 1$).

In order to study the system's temperature dependence, a system is taken from a high temperature of $T^* = 3$ (where the unconfined or infinite system is isotropic) into a low temperature of $T^* = 2.3$ (where the infinite system has turned columnar), through an annealing procedure with ΔT^* steps of 0.05, although a smaller ΔT^* steps of 0.02 were used for the region of temperatures where the systems present a nematic phase. Simulation runs consisted of $\mathcal{O}(10^6)$ time steps for equilibration for each T^*, followed by production runs of 1×10^7 timesteps. To minimize configurational correlations between measurements, thermodynamic and structural quantities were calculated every 100 timesteps, from which averages were then determined.

3 Results and discussion

3.1 Results

In what follows, results from simulations are presented for the DLC infinite system and four different confined systems: face-on anchoring systems with confinement length $L_z^* = 25$, and anchoring strengths of $\epsilon_w = 1$, 5, 10 and 15; the results of the unbounded system will be presented first, followed by those corresponding to all the confined systems.

In order to characterize the orientational order of the system, we calculated the largest eigenvalue of the orientational tensor [41]:

$$\mathbf{Q} = \frac{1}{2N}\sum_{i=1}^{N}(3\hat{\mathbf{u}}_i \bigotimes \hat{\mathbf{u}}_i - \mathbf{I}) \tag{12}$$

where $\bigotimes$ denotes the tensor product, $\mathbf{I}$ corresponds to the identity matrix, and N is the total number of particles contained in the system. The normalized eigenvector corresponding to λ_{max} is the system director $\mathbf{n}$, and $S = \lambda_{max}$ is referred to as the orientational order parameter. If $S = 0$ the liquid crystal is in an isotropic state. As the number of particles whose unit vector along their principal axis that are aligned with the director increases, the S increases up to reach a maximum value $S = 1$ which occurs when all the particles are perfectly aligned with the director.

The results for an annealing process of an unbounded system composed of 2000 discotic molecules at $P^* = 25$, were presented first by Bates and Luckhurst [34]. In figure 3 we show the results obtained with our code for the same system with 20000 particles inside of a cubic box of variable volume V, using a Nosé-Hoover thermostat/barostat couple with the same thermostat/barostat constants defined in the simulation details. It is important to state that the results presented in [34] and those obtained in our studies are practically identical, and, hence, results from Ref. [34] show no finite size effect. The general behaviour of the unbounded system were analyzed in detail inside of the above mentioned reference. Here we only show those results for facilitating the comparison between the unconfined and confined systems.

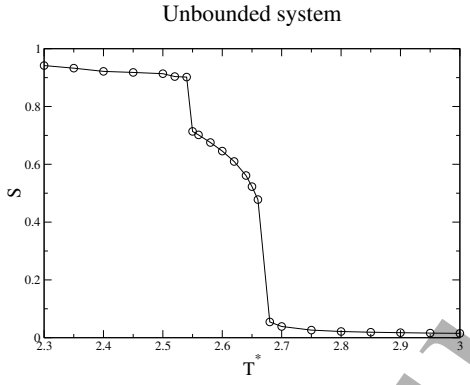

Figure 3: Order parameter vs reduced temperature calculated with NPT molecular dynamics simulations of the unbounded system with 20000 particles and $P^* = 25$.

With regard to the confined systems, a well known fact is that the anchoring induces an stratification of the fluid, forming ordered layers near the wall that gradually looses orientational and translational order as one moves away from the walls [28]. Since the systems under consideration are inhomogeneous due to the layering induced by the walls, then the orientational and positional order of the fluid will be position dependant. In this case, the value of the local orientational order parameter $S(z^*)$ is calculated on thin layers of normalized width 0.05 along the z direction, and corresponds to the largest eigenvalue of the time average of the orientational tensor $\mathbf{Q}$ on a given layer.

The results with the calculation of the order parameter for all the confined systems with $L_z^* = 25$ and face-on anchoring are shown in Fig. 4, where we plot S as a function of the distance z^*, for several values of T^*. The lowest temperature shown was determined by the first temperature value where the system presents a columnar phase.

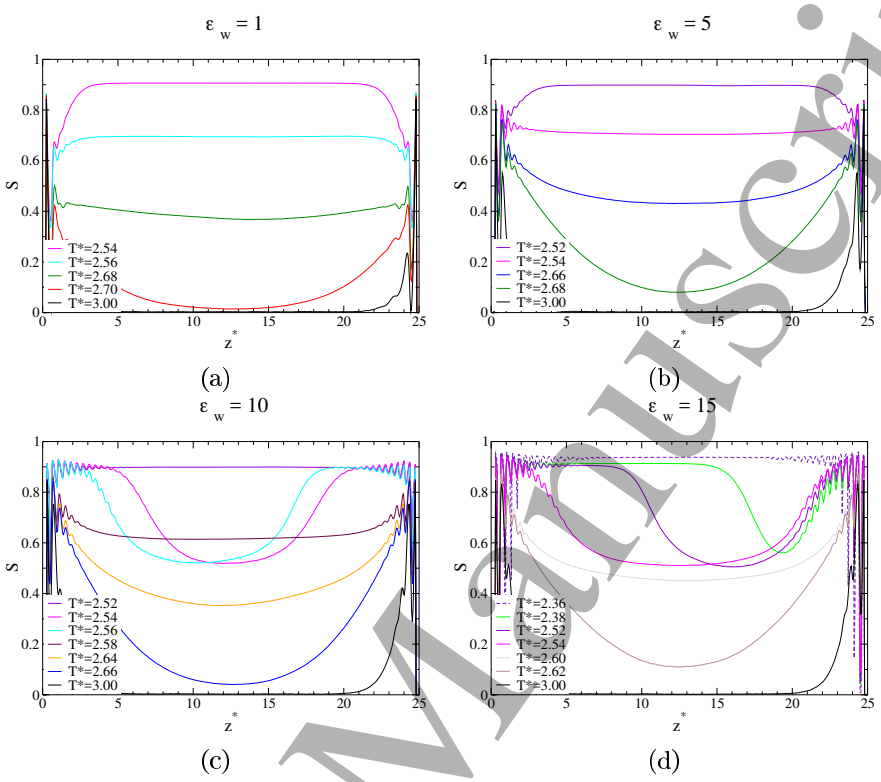

Figure 4: Results for the order parameter of the four confined systems: (a) lowest anchoring strength of $\epsilon_w = 1$, and temperature range of $T^* \in [2.54, 3.0]$, (b) anchoring strength of $\epsilon_w = 5$, and temperature range of $T^* \in [2.52, 3.0]$, (c) anchoring strength of $\epsilon_w = 10$, and temperature range of $T^* \in [2.52, 3.0]$, and (d) the highest anchoring strength used for this study with $\epsilon_w = 15$ and a temperature range of $T^* \in [2.36, 3.0]$. Although different temperatures are considered in each plot, notice that the same color scheme is used for all of them, for instance, in the four panels the black lines represent the temperature of $T^* = 3.0$ and the blue lines represent the temperature of $T^* = 2.66$.

Although the orientational order promoted by the walls is always higher adjacent to the walls for higher values of ϵ_w, the system where the isotropic-nematic transition happens first, this is, at the highest temperature, corresponds to the system with the lowest value of ϵ_w. Observe the green line in Fig 4a, which represents the S profile of the system where $\epsilon_w = 1$ at a temperature of $T^* = 2.68$, at this temperature the nematic phase is observed. Notice that at the same temperature, the systems where $\epsilon_w = 5$ and 10 present a lower order parameter at the center of the cell (green lines in 4b and 4c, respectively). This behaviour has a consequence in the isotropic-nematic transition temperature: the system where $\epsilon_w = 5$ presents a nematic phase first at $T^* = 2.66$; the system where $\epsilon_w = 10$ turns into nematic at $T^* \approx 2.64$ and, finally, the case with the higher anchoring strength turns nematic at $T^* \approx 2.60$. In other words,

although a strong anchoring induces a higher order parameter in the layers adjacent to a wall, the orientational order at the center of the cell decreases as this anchoring strength increases. This results in a lower isotropic-nematic transition temperature at the center of the cell for higher values of the anchoring strength.

With regard to the systems with lower anchoring strength ($\epsilon_w = 1$), a change in the curvature of the S profile occurs for temperatures below $T^* = 2.68$ (green line in Fig. 4a): the curve changes from concave to convex and it will remain with that shape at lower temperatures. The case with $\epsilon_w = 5$ shows a similar behaviour when turning from nematic to columnar ($T^* < 2.54$), as shown in Fig. 4b. In other words, for these temperatures, the fluid at the center of the cell possess a higher orientational order as compared to the fluid which is part of the interface. Further information about the positional order of the particles at a given distance from the wall, can be obtained via a quasi-two dimensional radial distribution function calculated for layers parallel to the wall. This radial distribution function can be defined as:

$$g(r_{xy}) = \frac{N(r_{xy})}{2\pi r_{xy} \mathrm{d}r_{xy}}, \tag{13}$$

where r_{xy} stands for the xy projection of the distance between two particles, $2\pi r_{xy}\mathrm{d}r_{xy}$ stands for the area of a cell, parallel to the wall, of thickness $\mathrm{d}r_{xy}$ and $N(r_{xy})$ is the number of particles inside this cell. Fig 5 includes the results for this pair correlation function calculated for $\epsilon_w = 1$ and at four different distances from the walls: $\Delta z^* = 0.35$ (black lines), 0.7 (red lines), 1.2 (green lines) and 1.5 (blue lines). Each layer thickness was set at $0.4\sigma_0$. Notice that at $T^* = 2.56$ (Fig 5 (a)), the shape of the curve for the four layers is similar, although more pronounced peaks can be distinguished for layers more distant from the wall. For lower temperatures this effect becomes more dramatic, and the fluid increases notably its positional order for the layers that are closer to the center of the cell. Observe, for example, the curves for $T^* = 2.4$ in Fig. 5 (d), where only the fluid in the two more distant layers (obtained for $\Delta z^* = 1.2$ and 1.5) are clearly in an hexagonal arrangement (green and blue lines, respectively).

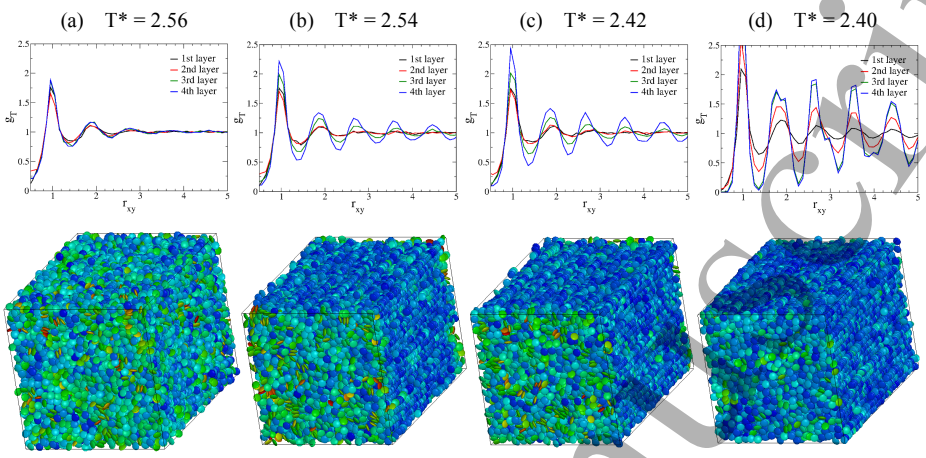

Figure 5: Results for the system with the lower anchoring strength ($\epsilon_w = 1$) at four different temperatures: (a) T* = 2.56, (b) T* = 2.54, (c) T* = 2.42 and (d) T* = 2.40. The upper row contains the results for the quasi-two-dimensional pair distribution function, calculated for four different layers parallel to the wall (see text for further details), and the lower row includes the corresponding snapshots of the system. The color code for the orientations of the mesogens is as follows: the blue particles have their orientation vector parallel to a vector normal to the wall, and red particles have orientation vectors perpendicular to the same reference direction. All snapshots presented in this work were obtained with the qmga software [42].

In the case of $\epsilon_w = 10$ and 15, the pair correlation function reflects an hexagonal arrangement at the interface, before it is observed at the system's bulk. The strongest anchoring induces first this arrangement: in the system with $\epsilon_w = 10$, $g(r_{xy})$ changes at $T^* = 2.56$ (Fig. 6a), and for the system with $\epsilon_w = 15$, $T^* = 2.58$ is the first temperature at which this characteristic hexagonal pattern is observed in the adsorbed layers (Fig. 6b). Another difference between the systems with lower anchoring strength, as compared to the two systems with a stronger anchoring, is related to the nematic-columnar transition. In the latter two cases there are temperature regions where a nematic-columnar coexistence is obtained. This coexistence temperature region is wider in the case where the value ϵ_w is bigger: when $\epsilon_w = 10$, there are only two temperatures where the coexistence is observed ($T^* = 2.56$ and 2.54), while for the case with $\epsilon_w = 15$, the coexistence region is observed in the temperature region of $T^* \in [2.38, 2.52]$.

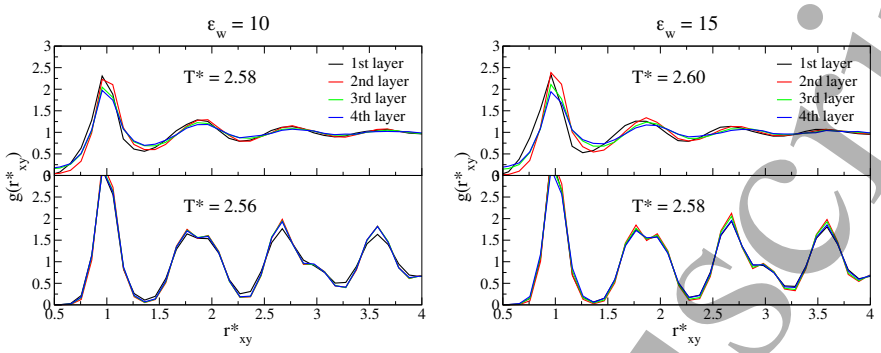

Figure 6: Results for the pair correlation function calculated for the systems with the stronger anchoring strength: (a) $\epsilon_w = 10$, at $T^* = 2.58$ and 2.56, and (b) $\epsilon_w = 15$, at $T^* = 2.60$ and 2.58. The pair correlation function is calculated at four different layers parallel to the wall: $\Delta z^* = 0.35$ (black line), 0.7 (red line), 1.2 (green line) and 1.5 (blue line).

Also useful for the structural characterization of the systems is the density profile. We calculated this quantity in the z^* direction using $\rho^*(z) = N_z/(A_{xy}dz)$, where N_z is the number of particles in a slab parallel to the wall, A_{xy} is the area of the box in the x-y plane and dz is the width of the bin, which in this case was also fixed at $0.05\sigma_0$. These results are shown in Fig. 7, where we plot ρ^* as a function of the distance z^*, for several values of T^*. The lowest temperature shown was determined by the last temperature value where the system presents a nematic phase; nematic-columnar coexistence and columnar phase temperatures were omitted in order to avoid confusion by too many lines in a single plot.

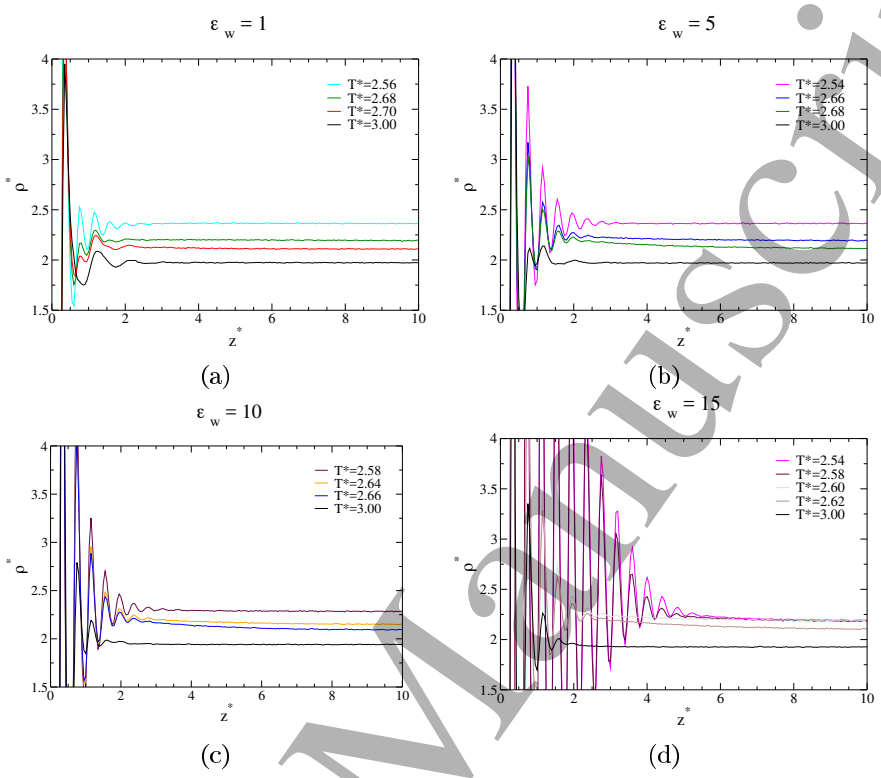

Figure 7: Profiles for the reduced density in the z direction of the four confined systems: (a) lowest anchoring strength of $\epsilon_w = 1$ and temperature range of $T^* \in [2.56, 3.0]$, (b) anchoring strength of $\epsilon_w = 5$ and temperature range of $T^* \in [2.54, 3.0]$, (c) anchoring strength of $\epsilon_w = 10$ and temperature range of $T^* \in [2.58, 3.0]$, and (d) the highest anchoring strength used for this study with $\epsilon_w = 15$ and a temperature range of $T^* \in [2.54, 3.0]$. Although different temperatures are considered in each plot, notice that the same color scheme is used for all of them, for instance, in the four panels the black lines represent the temperature of $T^* = 3.0$ and the blue lines represent the temperature of $T^* = 2.66$.

Notice the influence of the anchoring reflected through the presence of a succession of peaks in the density profile. As the intensity of the anchoring is increased the high of the peaks near the interface increases but without changing their location in the cell. The elastic forces between the DLC particles will induce successive layers, each one less crowded than the previous one as indicated by progressively lower peaks. Similarly, lowering the temperature increases the relevance of the potential energy between the particles and this promotes more ordered and densely packed regions which translates into higher peaks which in turn, translates into more particles at the interface and thus, less particles at the bulk (considering the bulk as the region where the density levels-off to a uniform value).

Fig. 8 shows the results of density profiles and their corresponding snapshots

for the system with the higher anchoring strength, at temperatures that span the beginning of the adsorbed layers up to the beginning of the nematic-columnar coexistence region. At $T^* = 2.58$, although there is an abrupt increase of the adsorbed layers, the density profiles remains with the characteristic profile of the interface. This changes at $T^* = 2.52$ where a flat region near to the left interface can be distinguished in the density profile. In other words, at these temperatures there are two flat regions distinguishable in the density profile, one with a nematic order parameter and the other with a columnar order parameter, and, hence, we labeled them as a nematic-columnar coexistence region.

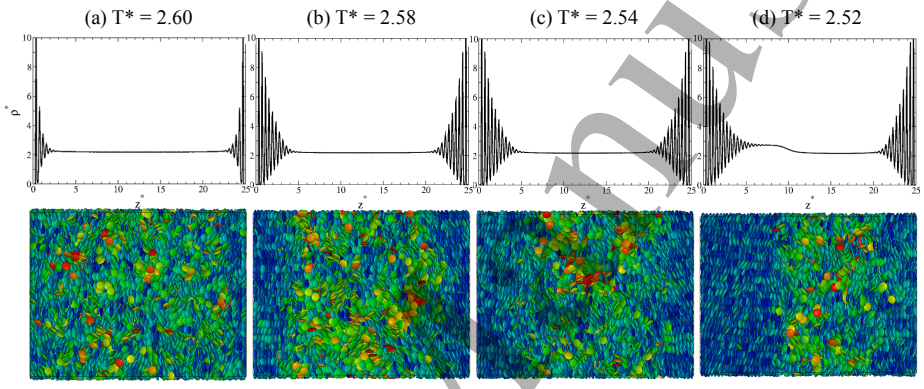

Figure 8: Results for the system with the stronger anchoring strength ($\epsilon_w = 15$) at four different temperatures: (a) T* = 2.60, (b) T* = 2.58, (c) T* = 2.54 and (d) T* = 2.52. The upper row contains the results of the density profile, while the lower row includes the corresponding snapshots of the system. The color codes of the snapshots as indicated in Fig. 5.

We quantified the layering in the isotropic and nematic regions by calculating the adsorption coefficient Γ_{ρ^*}, defined as:

$$\Gamma_{\rho^*} = \int_{z=0}^{L_z^*/2} (\rho^*(z^*) - \rho^{*B}) \mathrm{d}z, \tag{14}$$

where ρ^{*B} stands for the time average density at $z^* = L_z^*/2$. Figure 9 shows the values of Γ_{ρ^*} obtained for the range of temperatures of $T^* \in [2.54, 3.00]$, where, for all the anchoring strengths, there are two clearly defined regions: isotropic and nematic. Notice that the isotropic-nematic transition temperature decreases when increasing the anchoring strength. For instance: for $\epsilon_w = 1, 5, 10$ and 15 the isotropic region is obtained in the temperature ranges of $T^* \geq 2.7, 2.68, 2.66$ and 2.62, respectively. In these isotropic regions, Γ_{ρ^*} is expected to have positive values at high anchoring strengths due to the layering, whose average density is bigger than the bulk density. As the temperature is increased, eventually, the well of the wall potential becomes progressively irrelevant until the dominant effect is the depletion produce by the repulsive part of the wall potential. In this case the density near the wall is lower than the bulk density and, thus, Γ_{ρ^*}

becomes negative. This is clearly observed in the case where $\epsilon_w = 5$. In the case where $\epsilon_w = 1$ the anchoring strength is so small that the depletion effect dominates over the whole isotropic region, and therefore Γ_{ρ^*} is negative.

In the nematic region the behaviour is the opposite, i.e., Γ_{ρ^*} is an increasing function of T^*. To understand this let us notice that only the region close to the wall contributes significantly to the integral in Eq. 14. As can be seen in Fig. 7, the oscillatory behaviour of $\rho^*(z)$ in this region makes its contribution to the integral in Eq. 14, low sensitive to the value of T, thus, $\frac{\delta\Gamma_{\rho^*}}{\delta T} \approx -\frac{\delta\rho^B}{\delta T}\Delta z$, where Δz is the region near the wall. Since $\frac{\delta\rho^B}{\delta T} < 0$, then $\frac{\delta\Gamma_{\rho^*}}{\delta T} > 0$. An exception exists though, for the system with the stronger anchoring used ($\epsilon_w = 15$) presents a temperature region where a thin-thick layer transition is observed, and which was also clearly recognized in the density profiles of Fig. 7d. In this case, the drastic increment of layers adjacent to a wall promotes a bigger contribution of the first term in Eq. 14, and hence, in this region, Γ_{ρ^*} behaves as a decreasing function of T^*.

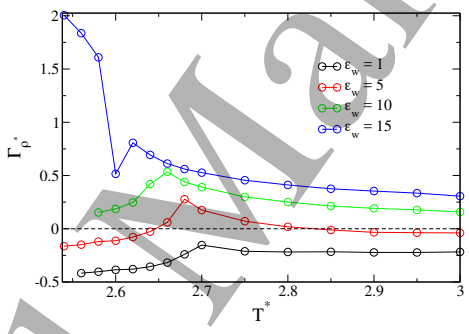

Figure 9: Adsorption coefficient Γ_{ρ^*} calculated at temperatures where the confined systems present isotropic and nematic phases, and for the four anchoring strengths studied: $\epsilon_w = 1, 5, 10$ and 15 are represented by the black, red, green and blue lines, respectively.

3.2 Discussion

Figures 10 and 11 present two regions of the T vs ρ^* space which summarizes the results of our study for the GB(0.5,0.2,1.0,2.0) fluid at $P^*_{xy} = 25$ and its comparison with the behaviour of the unconfined fluid. Fig. 10 contains the results for high temperatures, where all the systems present isotropic and nematic phases, while Fig. 11 contains the results for the lower temperatures up to $T^* = 2.3$, where all the systems have turned into a columnar phase.

At this point it is important to emphasize that our study is focused on the comparison of systems with a fixed confinement length, where only the tangential component $P^*_T = \frac{1}{2}(P_{xx} + P_{yy}) = 25$ of the stress tensor is fixed, and, hence, the direct comparison of an inhomogenous system where $P^*_T = 25$ versus an homogeneous system where $P^*_{xx} = P^*_{yy} = P^*_{zz} = p^* = 25$, is more qualitative than quantitative. Indeed, in these confined systems the pressure is not fixed

but rather only the average value of the tranverse component of the pressure P_T^*, which results in a different value of the normal component of the pressure $P_N^* = P_{zz}^*$. As expected [43], only far from the interface, where the bulk is recovered, all the elements of the diagonal of the stress tensor are equal. In our study for temperatures where the system presents isotropic and nematic phases, the biggest difference obtained between the tangential and normal components, at the bulk, is about $\sim \%0.6$, which could be fairly treated within the numerical error. Observe that for this temperature regions it is straightforward to delimit a region of the cell where the system's bulk is present. Our results indicate that, for temperatures where the nematic phase is present, the lower anchoring strength results in $P_N^* > 25$, while the other anchoring strengths result in a system with $P_N^* < 25$. Increasing the anchoring strength reduces the value of P_N^* in the system. Notice that, contrary to P_T^*, the normal pressure is independent of z^* for this inhomogeneous system. This is a good link between the behaviour observed at the system's bulk, for the isotropic and nematic regions, and the results for the normal pressure. For example, the system with the lower anchoring strength has a $P_N^* > 25$ and, hence, a density at the bulk slightly higher than that obtained for the unbounded system at $P^* = 25$. Also, the system with the higher anchoring strength has the lower value of P_N^* which results in the lower value of the bulk's density.

Figs. 10a and 10b show the average density calculated in two different ways: panel (a) shows the average in the whole cell, while panel (b) shows the average only in the central part of the cell ($z^* \in [10, 15]$), where the density is approximately constant. Notice that in Fig. 10a, at temperatures where all the systems remain in the isotropic phase $T^* \geq 2.7$, the average density shows no clear difference between any of the systems. This means that the equilibrium volume obtained, for a given temperature and a given tangential pressure component, is the same for all the systems if they remain in the isotropic phase at the bulk. When the bulk of the system changes from isotropic to nematic, the density changes abruptly, as can be seen from the density behaviour of the infinite system (black symbols in Fig. 10a). This changes the average density of the entire system.

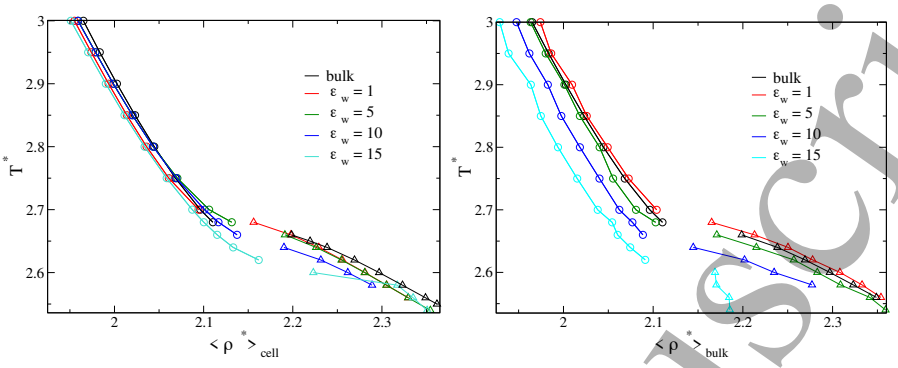

Figure 10: Region of the phase diagram where the unconfined and four confined systems are in the isotropic and nematic phases. The black lines represent the infinite system, while the red, green, blue and cyan lines stand for the confined systems with anchoring strength of $\epsilon_w = 1, 5, 10$ and 15, respectively. Open circles represent the isotropic phase and open triangles stand for the nematic phase. Two different regions used for the calculation of the average density are shown: a) shows the average density calculated over the entire cell, while in b) the average bulk density presented corresponds to value obtained at the central region of the cell: $z^* \in [10, 15]$.

Further understanding of the temperature depression of the Isotropic-Nematic transition, can be obtained by analyzing the behaviour of the density at the system's bulk: Fig 10b shows that for the unconfined system, the isotropic phase (black circles) is obtained for $T^* \gtrsim 2.68$ and the nematic phase (black triangles) is obtained for $T^* \in [2.54, 2.66]$. As compared to the infinite system, the two smaller anchorings do not modify significantly the isotropic-nematic transition temperature nor the width of the temperature regions where the nematic phase is present (blue and green lines represent the results for $\epsilon_w = 1$ and $\epsilon_w = 5$ systems, respectively. Circles stand for isotropic phase while triangles stand for nematic phase). For the system with $\epsilon_w = 1$, the lowest temperature where the isotropic phase is obtained, is slightly higher than the one obtained on the infinite system ($T^* = 2.7$ vs $T^* = 2.68$, respectively). This is the result of the depletion effect of the walls at this low attraction strength, which translates in a higher density at the bulk as compared to the unbounded system. This result is in accordance to what is observed for a system of hard spherocylinders confined between hard walls [44]. For $\epsilon_w = 5$, the system remains in the isotropic phase for $T^* \geq 2.66$, just as the infinite system. Notice that for the three above mentioned systems, both the density and order parameter have similar values in this temperature range. This relationship, where a higher order parameter is obtained for higher densities of the system, was observed in a previous numerical study on an inifinte system of prolate liquid crystals [45]. A stronger anchoring reduces the isotropic-nematic transition temperature, and results in a smaller nematic temperature region. When $\epsilon_w = 10$, the nematic region is delimited by $T^* \in [2.58, 2.64]$, while for the system with $\epsilon_w = 15$, the nematic region

is delimited by $T^* \in [2.54, 2.60]$. At the nematic phase, the system with the stronger anchoring shows a particularly small increment in the bulk's density when lowering the temperature. This was previously depicted by the reduced density curves shown in Fig. 9, and is the result of the layering at the walls which decreases the particles available to the nematic phase at the bulk.

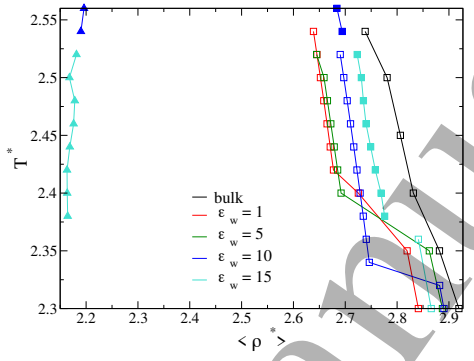

Figure 11: Region of the phase diagram that contains the results where the systems are in a nematic-columnar coexistence (nematic and columnar phase represented by filled triangles and filled squares, respectively), and in the columnar phase (open squares). The same color schemes of Fig. 10 are used. The average density of each phase at the nematic-columnar coexistence region was calculated by imposing arbitrary limits, in the z^* direction, that determine a region of the cell where the density profile remained constant. For systems where a single phase was obtained, the average density was calculated considering the entire cell.

In Fig. 11 the average density of each phase at the nematic-columnar coexistence region was calculated by imposing arbitrary limits in the z^* direction, that determine a region of the cell where the density profile remained constant. For temperatures below this coexistence region, the average was taken over the entire cell, this is, considering both the bulk and the interface. For temperatures below the nematic region the infinite system turns into columnar, and this phase is delimited by $T^* \leq 2.54$ (black squares). For the two weaker anchorings used, the system also turns from nematic to columnar when lowering the temperature. Explicitly, the system with $\epsilon_w = 1$ presents a columnar phase for $T^* \leq 2.54$ and for $\epsilon_w = 5$ a columnar phase is obtained for $T^* \leq 2.52$. However, notice that for the two higher values of the anchoring strengths, the nematic-columnar coexistence temperature-region is wide enough to be observed in our annealing process. Explicitly, when $\epsilon_w = 10$ we observed the coexistence for $T^* \in [2.54, 2.56]$, and when $\epsilon_w = 15$ the coexistence was observed for $T^* \in [2.38, 2.52]$. In other words, the nematic-columnar coexistence region is wider for the highest value used of the anchoring strength. For temperatures below the coexistence region, a pure columnar phase is obtained.

In order to compare our results with experimental data, here we present some estimates for the dimensionless parameters used in the simulations. First,

notice that all the interesting phenomena observed in this work is around $T^* \equiv k_B T/\epsilon_0 \simeq 3$. Assuming room temperature, then $\epsilon_0 \simeq 1.315 \times 10^{-21}$ Joules. With this energy value we can estimate the four anchoring energies, since the adsorption energy per particle, defined by the minimum of the wall-disc potential, is $|E_A| \simeq \alpha\epsilon_0$ with $\alpha \in \{1.5, 8, 15.5, 23\}$ (according to Fig. 2b, for the face-on case). In order to transform the surface energy density, let us consider the area of a nematogen in contact with a wall as approximately $A = \pi\sigma_0^2/4$ and a value of $\sigma_0 = 40$ Angstroms, which corresponds to the diameter of a triphenylene-based molecule [46]. This results on a surface energy density of $\alpha \times 10^{-4}$Joules$/m^2$. Substituting α with the highest and lowest value of 1 and 23, respectively, we obtain a minimum value of 1.6×10^{-4}Joules$/m^2$ and a maximum value of 2.5×10^{-3}Joules$/m^2$ for the surface density energy, both within the range of the highest experimental measured anchoring energy, where the experimental values range from $10^{-6} J/m^2$ to $10^{-3} J/m^2$ [17, 47]. With respect to the size of the cell, the reference value of the diameter of a triphenylene-based molecule results in $L_z = 25\sigma_0 = 100$ nm. Notice that this value is again near to the experimental values for confined liquid crystals, which range from confinement lengths of 10 nm to 200 nm [48, 49]. Finally, considering a value for the reduced pressure of $P^* \equiv P\sigma_0^3/\epsilon_0 \simeq 25$, results on an approximated pressure of 5.3×10^5 Pascals which is well within the reach of experiments done with liquid crystals under high pressure (8×10^7 according to reference [50]).

It is interesting to notice that for both type of systems, confined and unconfined, the system presents big density variations throughout the whole annealing process (Figs 10 and 11). This phenomenon is not observed in real LC systems where, for example, in the nematic-columnar transition the fractional change of volume is proportional to 1×10^{-3} [50]. In our case, the fractional change of volume on the same transition, is an order of magnitude higher. Although the Gay-Berne model is well known to accurately represent the mesophases observed in real molecular liquid crystals, and for many studies it has been parameterized with the reference of a particular real molecule (as our case, where a tryphenilene molecule was considered to adjust the Gay-Berne parameters), it is possible that specifically with regard to density behaviour, this model adjusts better to a model of colloidal liquid crystals rather than to molecular liquid crystals.

4 Conclusions

In this numerical study we have discussed the effects that the anchoring strength has on the mesophases of a discotic liquid crystal. We explored a slab geometry with a fixed length and a face-on anchoring, while four different depths in the disc-wall potential were considered. This was achieved by using an ensemble that kept fixed the distance between the walls and the tangential stress tensor components. Performing simulations on an ensemble where the confinement length is fixed forbid us from the possibility of comparing confined systems where the pressure is fixed. The chosen width of the slab allowed to clearly recognize the isotropic-nematic and nematic-columnar phase transitions. Using thinner

cells may have result in continuous transitions, instead of the discontinuous ones observed, as shown in references [21, 51].

Our results show that the anchoring has an impact on the nematic phase: when the anchoring strength is higher, the range of temperatures where this phase is present is reduced. In other words, a strong anchoring of the walls destabilizes the nematic phase in favour of the columnar phase. The corresponding transition temperature shows a clear behaviour in the confined systems: increasing the anchoring strength reduces the temperature at which the system turns to nematic. This is the result of studying a system where the distance between the walls is fixed. In such a system, the normal component of the pressure tensor depends on the value of the anchoring strength. Different values of the normal component of pressure tensor result on different equilibrium densities at the system's bulk, which in turn changes the order parameter in this region. Hence, when the anchoring strength is increased, the density at the bulk decreases, which in turn decreases the order parameter at the bulk. Notice that this result is, to some extent, counterintuitive, as the anchoring is promoting an orientational order near the wall, and it could be expected that this order were translated, via elastic forces, into a higher order parameter at the bulk. However, this is not the case, as an interplay happens between the interface and the bulk: not only does a higher anchoring increases the order around the wall, but also the number of particles at the interface, which in turn reduces the bulk's density. Reducing the density is translated into a lower order parameter.

The anchoring strength also has an noticeable impact on the confined systems at temperatures below the nematic phase region: the two systems with a stronger anchoring ($\epsilon_w = 10$ and 15) show a nematic-columnar coexistence region that is not observed in the two systems with a lower anchoring ($\epsilon_w = 1$ and 5). This is, increasing the anchoring strength widens the nematic-columnar coexistence temperature-region. In the system where $\epsilon_w = 15$, the adsorption coefficient shows a thin-thick film transition at the walls.

Conflicts of interest

There are no conflicts of interest to declare.

Acknowledgements

The IPICYT's Supercomputing National Center supported this research with the computational time grant TKII-R2018-DSB1. CIM acknowledges partial financial support from DGAPA-UNAM grant number IN-110516. EDH and DSB acknowledges partial financial support from CONACYT, Mexico through project FDC2015-02-1450. We also thank the supercomputing resources provided by DGTIC-UNAM and UAM at Mexico City, Mexico.

References

[1] G. H. Heilmeier and L. A. Zanoni, *Appl. Phys. Lett.*, **13**, 91 (1968).

[2] Valery Shibaev, Alexey Bobrovsky and Natalia Boiko, *Prog. Polym. Sci.*, **28**, 729-836 (2003).

[3] Iam Choon Khoo, *Physics Reports*, **471**, 221-267 (2009).

[4] Manish Kumar and Sandeep Kumar, *Polymer Journal*, **49**, 85-111 (2017).

[5] A. Sengupta, *International Journal of Molecular Sciences*, **14**, 22826-22844 (2013).

[6] A. Sengupta, S. Herminghaus, and C. Bahr, *Liquid Crystals Reviews*, **2**, 73-110 (2014).

[7] Rui Zhang, Tyler Roberts, Igor S. Aranson, and Juan J. de Pablo, *J. Chem. Phys.*, **144**, 084905 (2016).

[8] René van Roij, Marjolein Dijkstra and Robert Evans, *J. Chem. Phys.*, **113**, 7689-7701 (2000).

[9] K. Kocevar, A. Borstnik, I. Musevic, and S. Zumer, *Phys. Rev. Lett.*, **86**, 5914 (2001).

[10] Paul E. Brumby, Henricus H. Wensink, Andrew J. Haslam and George Jackson, *Langmuir*, **33**, 11754-11770 (2017).

[11] Matthias Bremer, Peer Kirsch, Melanie Klasen-Memmer and Kazuaki Tarum, *Angew. Chem. Int. Ed.*, **52**, 8880-8896 (2013).

[12] Daniel Franklin, Yuan Chen, Abraham Vazquez-Guardado, Sushrut Modak, Javaneh Boroumand, Daming Xu, Shin-Tson Wu and Debashis Chanda, *Nature Communications*, **6**, 7337 (2015).

[13] Y. J. Liu and X. W. Sun, *Applied Physics Letters*, **90**, 191118 (2007).

[14] Thomas Gruhn and Martin Schoen, *Molecular Physics*, **93**, 681 - 692 (1998).

[15] Manuel Greschek, Michael Melle and Martin Schoen, *Soft Matter*, **6**, 1898-1909 (2010).

[16] Enrique Cañeda-Guzmán, José A. Moreno-Razo, Enrique Díaz-Herrera and Eduard J. Sambriski, *Molecular Physics*, **112**, 1149-1159 (2014).

[17] Mohammad Rahimi, Tyler F. Roberts, Julio C. Armas-Pérez, Xiaoguang Wang, Emre Bukusoglu, Nicholas L. Abbott, and Juan J. de Pablo, *PNAS*, **112**, 5297-5302 (2015).

[18] Julio C. Armas-Pérez, Xiao Li, José A. Martínez-González, Coleman Smith, J. P. Hernández-Ortiz, Paul F. Nealey, and Juan J. de Pablo, *Langmuir*, **43**, 12516-12524 (2017).

[19] Luis F. Rull and José M. Romero-Enrique, *Langmuir*, **33**, 11779-11787 (2017).

[20] D. Caprion, *Eur. Phys. J. E*, **28**, 305-313 (2009).

[21] Rémi Busselez, Carole V. Cerclier, Makha Ndao, Aziz Ghoufi and Ronan Lefort, *J. Chem. Phys*, **141**, 134902 (2014).

[22] Manuel M. Pineiro, Amparo Galindo and Andrew O. Parry, *Soft Matter*, **3**, 768-778 (2007).

[23] Kathrin Sentker, Arne W. Zantop, Milena Lippmann, Tommy Hofmann, Oliver H. Seeck, Andriy V. Kityk, Arda Yildirim, Andreas Schönhals, Marco G. Mazza, and Patrick Huber, *Phys. Rev. Lett.*, **120**, 067801 (2018).

[24] L. Bellier-Castella, D. Caprion, D., J.-P. Ryckaert, *J. Chem. Phys.*, **121**, 4874-4883 (2004).

[25] Sergey Sergeyev, Wojciech Pisula and Yves Henri Geerts, *Chem. Soc. Rev.*, **36**, 1902-1929 (2007)

[26] Cheng Zou, Jingxia Wang, Meng Wang, Yuchen Wu, Kehua Gu, Zhihao Shen, Guirong Xiong, Huai Yang, Lei Jiang and Tomiki Ikeda, *Small*, **14**, 1800557 (2018).

[27] Tobias Wöhrle, Iris Wurzbach, Jochen Kirres, Antonia Kostidou, Nadia Kapernaum, Juri Litterscheidt, Johannes C. Haenle, Peter Staffeld, Angelika Baro, Frank Giesselmann and Sabine Laschat, *Chemical Reviews*, **116**, 1139-1241 (2016).

[28] B. Jerôme, *Rep. Prog. Phys.*, **54**, 391-451 (1991).

[29] Takahiro Seki, Shusaku Nagano and Mitsuo Hara, *Polymer*, **54**, 6053-6072 (2013).

[30] Johan Hoogboom, Johannes A. A. W. Elemans, Theo Rasing, Alan E. Rowan and Roeland J. M. Nolte, *Polymer International*, **56**, 1186-1191 (2007).

[31] Youngwoo Yi, Michi Nakata, Alexander R. Martin and Noel A. Clark, *Appl. Phys. Lett.*, **90**, 163510 (2007).

[32] Douglas J. Cleaver, Christopher M. Care, Michael P. Allen, and Maureen P. Neal, *Physical Review E*, **54**, 559-567 (1996).

[33] Bates, M. A. and Luckhurst, G. R., *J. Chem. Phys.*, **110**, 7087-7108 (1999).

[34] Bates, M. A. and Luckhurst, G. R., *J. Chem. Phys.*, **104**, 6696 (1996).

[35] K. Kocevar and I. Musevic, *Liquid Crystals Today*, **112**, 3-8 (2003).

[36] A. Marino, V. Tkachenko, E. Santamato, N. Bennis, X. Quintana, J. M. Otón and G. Abbate, *Journal of Applied Physics*, **107**, 073109 (2010).

[37] Jaroslav M. Ilnytskyi and Mark R. Wilson, *Computer Physics Communications*, **148**, 43-58 (2002).

[38] Toshiki Mima and Kenji Yasuoka, *Physical Review E*, **77**, 011705 (2008).

[39] Toshiki Mima, Tetsu Narumi, Shun Kameoka and Kenji Yasuoka, *Molecular Simulation*, **34**, 761-773 (2008).

[40] Zerihun G Workineh and Alexandros G Vanakaras, *J. Phys.: Condens. Matter*, **28**, 115002 (2016).

[41] R. Eppenga and D. Frenkel, *Molecular Physics*, **52**, 1303 - 1334 (1984).

[42] Adrian T. Gabriel, Timm Meyer, Guido Germano, *J. Chem. Theory Comput.*, **4**, 468-476 (2008).

[43] J. S. Rowlinson and B. Widom, *Molecular Theory of Capillarity*; Dover Publications: Mineola, New York, 2002.

[44] Mehri Aghaei Semiromi and Abolghasem Avazpour, *Liquid Crystals*, **2**, 262-269 (2017).

[45] J. W. Emsley, G. R. Luckhurst, W. E. Palket and D. J. Tildesley, *Liquid Crystals*, **11**, 519-530 (1992).

[46] Santanu Kumar Pal, Shilpa Setia, B. S. Avinash and Sandeep Kumar, *Liquid Crystals*, **40**, 1769-1816 (2013).

[47] O. Lavrentovich, B. Lev and A. Trokhymchuk, *Condensed Matter Physics*, **13**, 30101 (2010).

[48] Giovanni Carbone, Giuseppe Lombardo, Riccardo Barberi, Igor Musevic and Uros Tkalec, *Physical Review Letters*, **103**, 167801 (2009).

[49] Ruibin Zhang, Xiangbing Zeng, Bongseock Kim, Richard J. Bushby, Kyusoon Shin, Patrick J. Baker, Virgil Percec, Pawaret Leowanawat, and Goran Ungar, *ACS Nano*, **9**, 1759-1766 (2015).

[50] Richard V. Tranfield and Peter J. Collins, *Physical Review A*, **25**, 2744-2749 (1982).

[51] D. Salgado-Blanco, C. I. Mendoza, J. A. Moreno-Razo, M. A. Chávez-Rojo and E. Díaz-Herrera, *Soft Matter*, **14**, 2846 (2018).